Turkish Journal of Electrical Engineering & Computer Sciences

http://journals.tubitak.gov.tr/elektrik/

Research Article

Turk J Elec Eng & Comp Sci
(2018) 26: 2287 – 2300

doi:10.3906/elk-1709-88

Image reconstruction for frequency-domain diffuse optical tomography

Vicky MUDENG*, **Yun PRIYANTO**, **Andhika GIYANTARA**
Department of Electrical Engineering, Kalimantan Institute of Technology, Balikpapan, Indonesia

Received: 11.09.2017 • **Accepted/Published Online:** 29.04.2018 • **Final Version:** 28.09.2018

Abstract: The image reconstruction algorithm of diffuse optical tomography (DOT) is based on the diffusion equation and involves both the forward problem and inverse solution. The forward problem solves the diffusion equation using the finite element method for calculating the transmitted light distribution under the condition of presumed light source and optical coefficient. The inverse solution reconstructs the optical property coefficient distribution using Newton's method. The work within this study develops an image reconstruction algorithm for frequency-domain DOT. A numerical simulations approach to light propagation in the tissue is conducted, while the optical property is reconstructed employing data around the boundary. We implement different designated simulation cases, including different contrast ratios of absorption and reduced scattering coefficient of inclusion with respect to the background used for verifying the results of the forward problem and the developed reconstruction algorithm. Reconstruction results indicate that the quality of reconstructed images can be effective for screening breast cancer.

Key words: Diffuse optical tomography, frequency domain, image reconstruction

1. Introduction

Diffuse optical tomography (DOT) refers to the imaging of biological tissue in the diffusive regime by using near-infrared (NIR) light [1]. Typically, the goal of DOT is to accurately estimate the distribution of optical properties in a tissue volume from noninvasive optical measurements on the surface of the medium [2]. Furthermore, its clinical application for imaging breast cancer is beginning to demonstrate functional information, such as oxy-hemoglobin and de-oxyhemoglobin, for screening [3,4]. As is known, NIR DOT produces low-resolved images, which limits its further clinical application due to highly scattered photon fields. In addition, an NIR DOT focus in regards to two issues, a forward measurement system [5] and a reconstruction algorithm [6,7], was primarily related to a measuring device and numerical computation software, respectively. Hence, the low-resolution drawback due to the ill-posed nature of the inverse problem can be improved by either a novel hardware design such as using multimodality, optical fibers optimization around the tissue boundary, or an innovative computational approach such as constraints in the image reconstruction, introducing prior information, varying parameters, or filtering techniques [8].

The circular array [9,10] is the most popular model geometry for imaging the breast in two dimensions, which drew researchers' attention. Some studies have been developed for two-dimensional image reconstruction to reflect a better understanding. Various algorithms can be utilized to estimate optical properties in DOT techniques. The decision of these algorithms is based on the photon propagation model, optimization scheme, measurement type, and geometry. A system using a multiwavelength scheme was applied to reconstruct better-

*Correspondence: mudengvicky@itk.ac.id

quality images such as a low cross-talk or high-contrast separability between the embedded tumor and the background [11,12]. Furthermore, the optimization of wavelength [13] to determine proper spectral ranges was developed, and the laser wavelengths' determination has a strong effect on maximizing optical properties accuracy [14].

Multimodality schemes have also been proposed for medical applications or clinical trials. Diffuse optical imaging along with coregistered X-ray systems generated a better performance between the functional and structural contrasts [15,16], with integration of an ultrasound probe and an NIR DOT for the solid lesion detection [17–19], or employed a combination of nuclear magnetic resonance imaging/magnetic resonance imaging (NMR imaging/MRI) and NIR imaging systems to be implemented an image guided for reconstructing NIR DOT [20,21], where such a hybrid imaging scheme was examined with an NIR image reconstruction algorithm usually incorporating a priori structural information provided by X-ray imaging, ultrasound imaging, or MRI systems.

On the other hand, to provide accurate information of the tissue, several studies were conducted. Reducing the imaging artifact in measurements due to probe-tissue coupling, patient and probe motions, and tissue heterogeneity were investigated by an automated method of outlier removal, data selection, and filtering for DOT [22]. In the discussion of wavelength optimization with a selection from commercial laser diodes to obtain more information of chromophores [14] and to allow bulk parameter recovery from measured spectra, a set of libraries based on a numerical model of the domain being investigated was developed as opposed to the conventional approach of using an analytical semiinfinite slab approximation, which was shown to introduce boundary effects [23].

In this study, we present the implementation of a finite element-based algorithm to provide forward calculation for the image reconstruction process. Due to the ill-posed nature of the inverse problem, Tikhonov regularization (TR) is utilized to stabilize the reconstruction results. Based on the algorithm, preliminary simulation results for reconstructing optical properties (such as absorption and reduced scattering coefficient) in the tissue are illustrated.

According to the above introduction, the organization of this paper is as follows. In Section 2, we describe the forward problem of DOT and light propagation is modeled; in addition, we state the inverse solution for image reconstruction and the estimation of optical properties in tissue. Subsequently, the simulation results of the forward problem and inverse solution are demonstrated in Section 3, where discussions are provided as well. Finally, some remarks and conclusions of the study are stated in Section 4.

2. Forward and inverse models

Estimating the distribution of the optical properties in tissue through the light propagation around a model boundary is the aim of DOT. A forward model is needed to show the relation between light radiance distribution on the tissue boundary and the exact optical properties for the objective of determining the reconstructed optical properties' images.

The inverse problem in image reconstruction for DOT is nonlinear but we can linearize this nonlinear problem by using first-order Taylor series and this can be done iteratively using Newton's method as shown in the following discussion, and then the nonlinear image reconstruction problem can be solved by a series of linear steps. However, these linear steps involve the Jacobian matrix, which needs to be constructed explicitly.

To express the above explanations in theory, a forward problem in DOT is first described in Section 2.1,

and then the use of the regularization method in an inverse problem is explained in Section 2.2, where TR is presented. Following that, the approach implemented in the numerical way is described in Section 2.3.

2.1. Forward problem

Time harmonic light propagation in tissues can be described by the well-known diffusion equation when tissues act as a highly scattering medium:

$$\nabla \cdot D \nabla \Phi(\boldsymbol{r},\omega) - \left(\mu_a - \frac{i\omega}{c}\right) \Phi(\boldsymbol{r},\omega) = -S_0(\boldsymbol{r},\omega) \tag{1}$$

where $\Phi(\boldsymbol{r},\omega)$ is the radiance, ω is the light modulation frequency, D is the diffusion equation, μ_a is the absoption coefficient, c is the wave speed in the medium, and $S_0(\boldsymbol{r},\omega)$ is the source term. The diffusion coefficient D can be written as:

$$D = \frac{1}{3\left[\mu_s(1-g)+\mu_a\right]} = \frac{1}{3\left(\mu_s^{'}+\mu_a\right)} \tag{2}$$

where μ_s is the scattering coefficient, g is average cosine of the scattering angle, and $\mu_s^{'}$ is the reduced scattering coefficient.

The use of the finite element method (FEM) to model the diffusion equation is attractive due to the flexibility in terms of geometry and the ability to preserve the nonlinear relationship between the measurements and optical properties in the diffusion equation. In order to simulate the light propagation by diffusion equation, we first must define the light source $S_0(\boldsymbol{r},\omega)$, boundary condition, and optical coefficients μ_a and $\mu_s^{'}$ in the model. In this study, the mixed boundary condition [24] is implemented as in Eq. (3). The FEM can be divided into two steps. First, the boundary condition is substituted into a weak form. Secondly, the Galerkin method along with a boundary condition is implemented:

$$-D\nabla\Phi.\hat{n} = \alpha\Phi, \tag{3}$$

where α is a term that incorporates reflection as a result of refractive-index mismatch at the boundary and $\hat{n}$ is the unit vector normal to the boundary. Thus, the following discrete equations in a matrix form,

$$\begin{bmatrix} \boldsymbol{A}_{ij}^{bb} - \alpha \boldsymbol{B}_{ij}^{bb} & \boldsymbol{A}_{ij}^{bI} \\ \boldsymbol{A}_{ij}^{Ib} & \boldsymbol{A}_{ij}^{II} \end{bmatrix} \begin{Bmatrix} \boldsymbol{\Phi}_j^b \\ \boldsymbol{\Phi}_j^I \end{Bmatrix} = \begin{Bmatrix} \boldsymbol{S}_j^b \\ \boldsymbol{S}_j^I \end{Bmatrix} \tag{4}$$

can be obtained. Here, b is the boundary node and l is the internal node. Obviously, the forward solution, $\boldsymbol{\Phi}$, can be evaluated with Eq. (4).

2.2. Inverse solution

Since the goal of DOT is to reconstruct the optical coefficient maps of the tissue, we can estimate this distribution by minimizing the misfit differences of data model,

$$\chi^2 = \|\Delta\Phi\|_2^2 = \left\|\Delta\Phi^M - \Delta\Phi^C\right\|_2^2 \tag{5}$$

which is minimal, where Φ^M is the measured photon density around the medium being investigated and Φ^C is the computed model data from solving the diffusion equation with the current estimated optical properties.

These data-model misfit differences can then be minimized by solving $\boldsymbol{J}\Delta\boldsymbol{\chi} = \Delta\boldsymbol{\Phi}$ iteratively, where $\boldsymbol{J} = \left[\partial\Phi^C/\partial\boldsymbol{\mu}_a\, \partial\Phi^C/\partial\boldsymbol{D}\right]$ is the Jacobian matrix, i.e. the rate of change of model data with respect to optical parameters, and $\Delta\boldsymbol{\chi}$ denotes the optical coefficient update vector $[\Delta\boldsymbol{\mu}_a; \Delta\boldsymbol{D}]$ at each iteration.

However, solving this inverse problem of $\boldsymbol{I}\Delta\boldsymbol{\chi} = \Delta\boldsymbol{\Phi}$ usually runs into the difficulty of an ill-conditioned problem as the number of model parameters (optical coefficients here) increases. Alternatively, TR is introduced to remedy such an issue. In TR, the inverse problem in DOT is formulated as an optimization of the damped least-squares problem [25]:

$$\left\{\|\boldsymbol{I}\Delta\boldsymbol{\chi} - \Delta\boldsymbol{\Phi}\|_2^2 + \lambda^2 \|\Delta\boldsymbol{\chi}\|_2^2\right\}, \tag{6}$$

where λ is a regularization parameter. One can minimize this damped least-squares problem by iteratively solving the following update equation:

$$\left(\boldsymbol{I}^T\boldsymbol{I} + \lambda^2 I\right)\Delta\boldsymbol{\chi} = \boldsymbol{I}^T\Delta\boldsymbol{\Phi} \tag{7}$$

2.3. Image reconstruction for DOT

In this study, the numerical computation was implemented in the model using repeated iteration. The flowchart for image reconstruction is shown in Figure 1. First, we assumed the distribution of optical properties in the model, and then the corresponding light source intensity was obtained in the forward calculation. The FEM solved the diffusion equation to obtain the light intensity and phase shift of the measurement nodes around boundary. As explained in Section 2.2, we calculated the solution of the diffusion equation and least-squares minimization error function (χ^2) as the criteria. If the error was greater than the initial estimation, then the inverse problem would be employed. In the inverse problem, we obtained optical properties' update values for each node. Then the optical properties obtained above were applied to the forward problem calculation, and the error was obtained again. These processes would be repeated until the stop criterion was met.

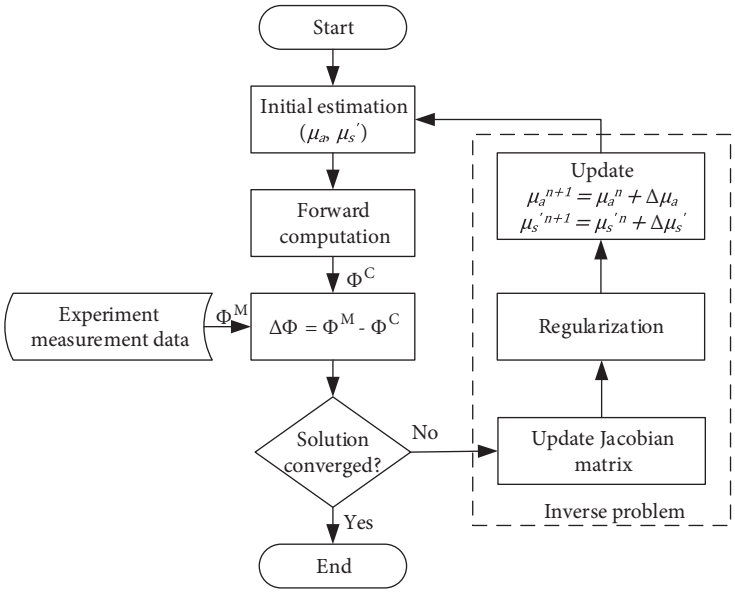

Figure 1. Flowchart for image reconstruction of DOT.

3. Results and discussion

This section describes how to produce simulated data as well as image reconstruction results. In order to test the image reconstruction algorithm, the simulation was employed first by using model information in the testing model. According to the actual shape of the breast and internal physiological information, we first had to assume the absorption (μ_a) and reduce scattering $\left(\mu_s^{'}\right)$ coefficients in the model. Then we used the FEM to simulate light distribution in the model and light intensity at the boundary. In addition, there were multiple light sources and measurement nodes for image reconstruction. In this study, we used a circular array as the model geometry with diameter of 80 mm. It was assumed that there were 16 light sources and 16 measurement nodes distributed along the boundary; therefore, there were 256 $(= 16\times16)$ measurements in total for reconstruction. To obtain simulated data, we used a group of finite element mesh with 4225 nodes and 8192 triangle elements for the inverse solution. The model geometry along with the light source and detector arrangement are shown in Figure 2a, while Figure 2b depicts the inclusion location inside the model.

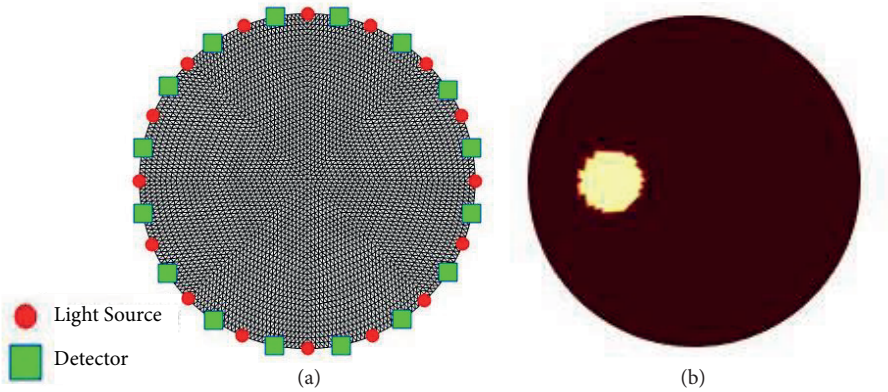

Figure 2. Model geometry to (a) show the arrangement of light sources (in red) and detectors (in green) on the boundary and (b) demonstrate the inclusion location.

Moreover, we assumed that μ_a and $\mu_s^{'}$ of the background in the model geometry were $0.01\,mm^{-1}$ and $1\,mm^{-1}$, respectively. We tried to simulate the model with different optical properties for the same size and location of inclusion, as shown in Table 1. Figures 3a–3d show the light radiance distribution for light sources 1, 5, 9, and 13, respectively. As can be seen, the light intensity was distributed well inside the model through our simulation. Forward solutions where predicted boundary data (intensity and phase) are plotted for homogeneous and inhomogeneous areas for $\mu_a = 0.02\,mm^{-1}$ and $\mu_s^{'} = 0.89\,mm^{-1}$ of inclusion are shown in Figure 4a for light source 1, as well as Figure 4b, Figure 4c, and Figure 4d for light sources 5, 9, and 13, respectively. On the other hand, Figures 5a–5d depict the predicted boundary data for $\mu_a = 0.02\,mm^{-1}$ and $\mu_s^{'} = 2\,mm^{-1}$ of inclusion. The modulation frequency was selected to be $100\,MHz$.

Figures 4a–4d and 5a–5d indicate the differences of light intensity and phase shift between homogenous and inhomogeneous areas where a single light source was applied. As predicted, the boundary data were affected by light source and inclusion position as well as optical properties of inclusion. These results of the forward solution prove the forward problem algorithm, promising to obtain simulation data for the image reconstruction next step.

Table 1. Different designated simulation cases with $\mu_a = 0.01\,mm^{-1}$ and $\mu_s^{'} = 1\,mm^{-1}$ of the background for single inclusion.

Case	Inclusion diameter (mm)	Inclusion location (x, y mm)	$\mu_a\,(mm^{-1})$	$\mu_s^{'}\,(mm^{-1})$
A1	15	–20, 0	0.02/0.025/0.03	0.89
A2	15	–20, 0	0.02	2/2.5/3

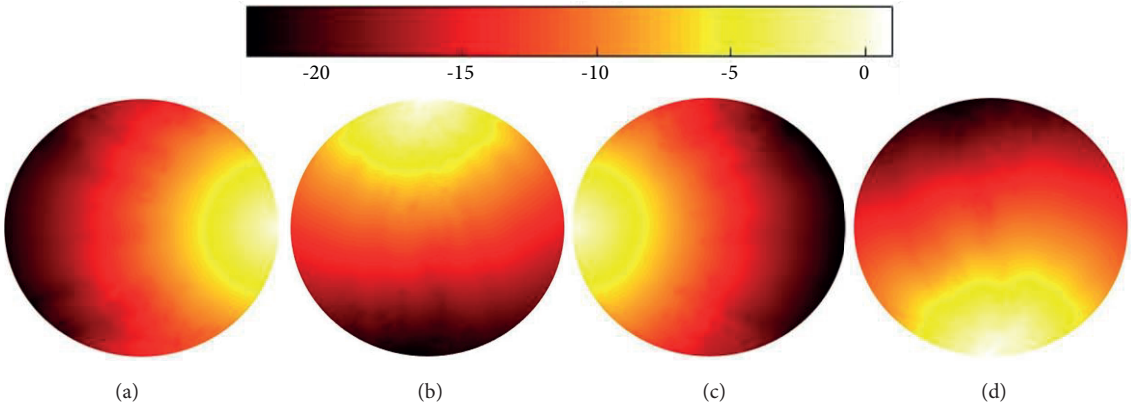

Figure 3. Radiance distribution for light sources (a) 1, (b) 5, (c) 9, and (d) 13.

In order to avoid inverse crime [26], we utilized different numbers of elements and nodes in the forward and inverse models, as shown in Figures 6a and 6b, respectively. To obtain reconstructed images in this study, we used a group of finite element mesh with 817 nodes and 1536 triangle elements for the inverse solution.

Figures 7 and 8 demonstrate simulated reconstructions of both the absorption and the reduced scattering images and the corresponding comparisons between exact and estimated reconstruction line profiles for different contrasts of μ_a but the same $\mu_s^{'}$, respectively. The reconstructed images and line profiles with different contrasts of $\mu_s^{'}$ but the same μ_a are shown in Figure 9 and 10, respectively. Comparing Figures 7 and 9, the reconstructed images show that greater inclusion contrast in the exact condition, with higher differences between inclusion and background for reconstructed results. Also, Figures 8 and 10 provide a more detailed assessment of these images by circular profiles through the inclusion center with a radius of 15 mm. We found for case A1 that with the greater μ_a of inclusion in the exact condition, the greater $\mu_s^{'}$ for inclusion with respect to the background in the reconstructed image was even overestimated. Otherwise, underestimation occurred for μ_a. Furthermore, underestimation of the optical properties' reconstructed images for each contrast ratio in case A2 occurred.

Additionally, we simulated simultaneously the conditions given in Table 2. These cases were specified with the optical-property values of $\mu_s^{'} = 0.89\,mm^{-1}$ and $\mu_a = 0.02$, 0.025 and $0.03\,mm^{-1}$ for the right, top, and left inclusion in case B1, respectively. On the other hand, we computed a $\mu_a = 0.02\,mm^{-1}$ and $\mu_s^{'} = 2,\ 2.5$ and $3\,mm^{-1}$ for the right, top, and left inclusion in case B2, respectively. The reconstructed images with three inclusions shown in Figure 11 clearly demonstrate that μ_a and $\mu_s^{'}$ reconstructed can be obtained by use of the algorithm in this study. Furthermore, Figure 12 depicts the circular profiles of image assessments through the three inclusion centers with a radius of 15 mm. Obviously, case B2 has higher contrast compared with case B1.

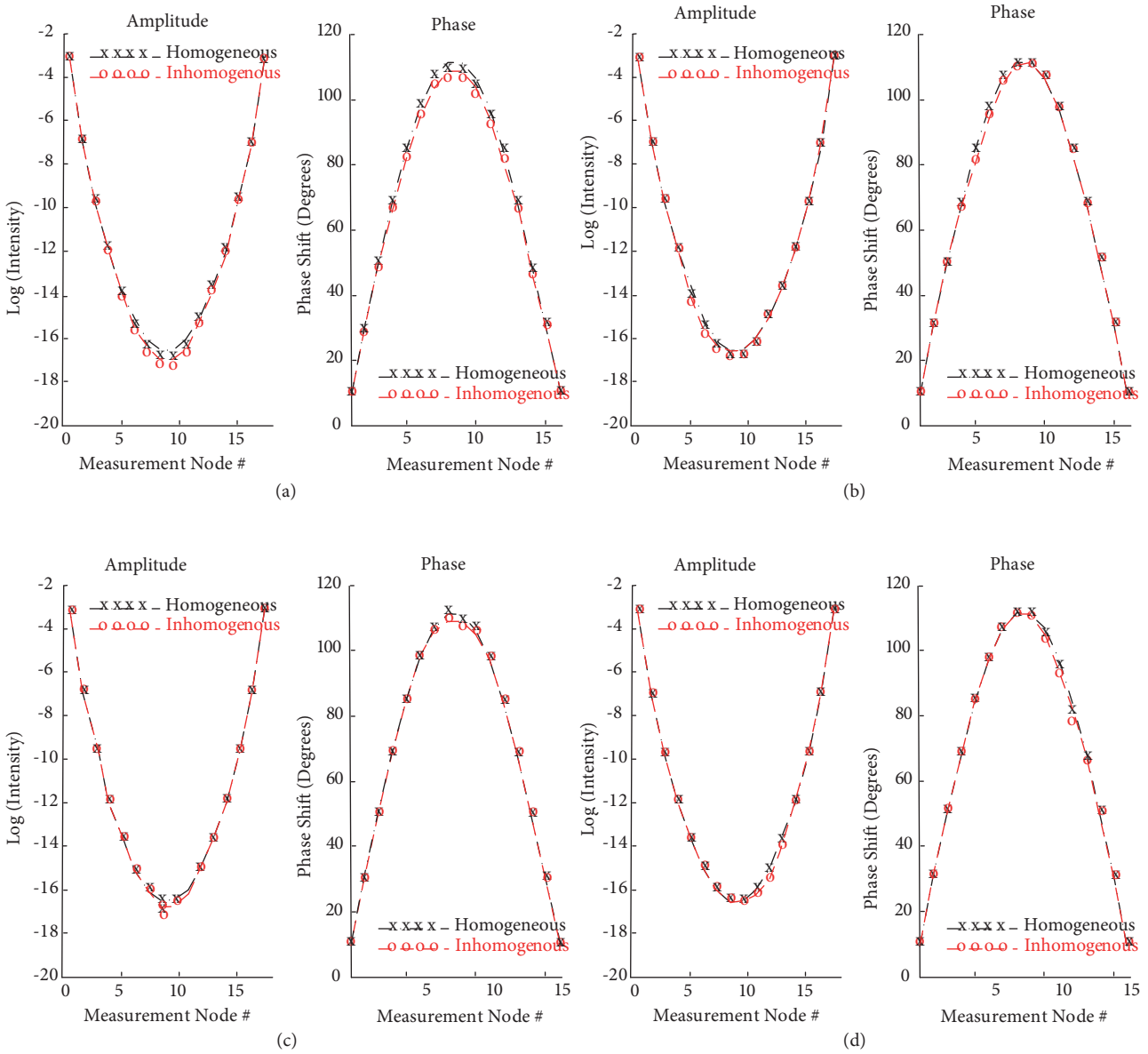

Figure 4. Computed light intensity and phase shift for $\mu_a = 0.02\,mm^{-1}$ and $\mu_s^{'} = 0.89\,mm^{-1}$ of inclusion: light sources (a) 1, (b) 5, (c) 9, and (d) 13.

Table 2. Same caption as Table 1 but for three different inclusion locations and contrasts.

Case	Inclusion diameter (mm)	Inclusion location (x, y mm)	$\mu_a\,(mm^{-1})$	$\mu_s^{'}\,(mm^{-1})$
B1	15	20, 0/0, 20/–20, 0	0.02/0.025/0.03	0.89
B2	15	20, 0/0, 20/–20, 0	0.02	2/2.5/3

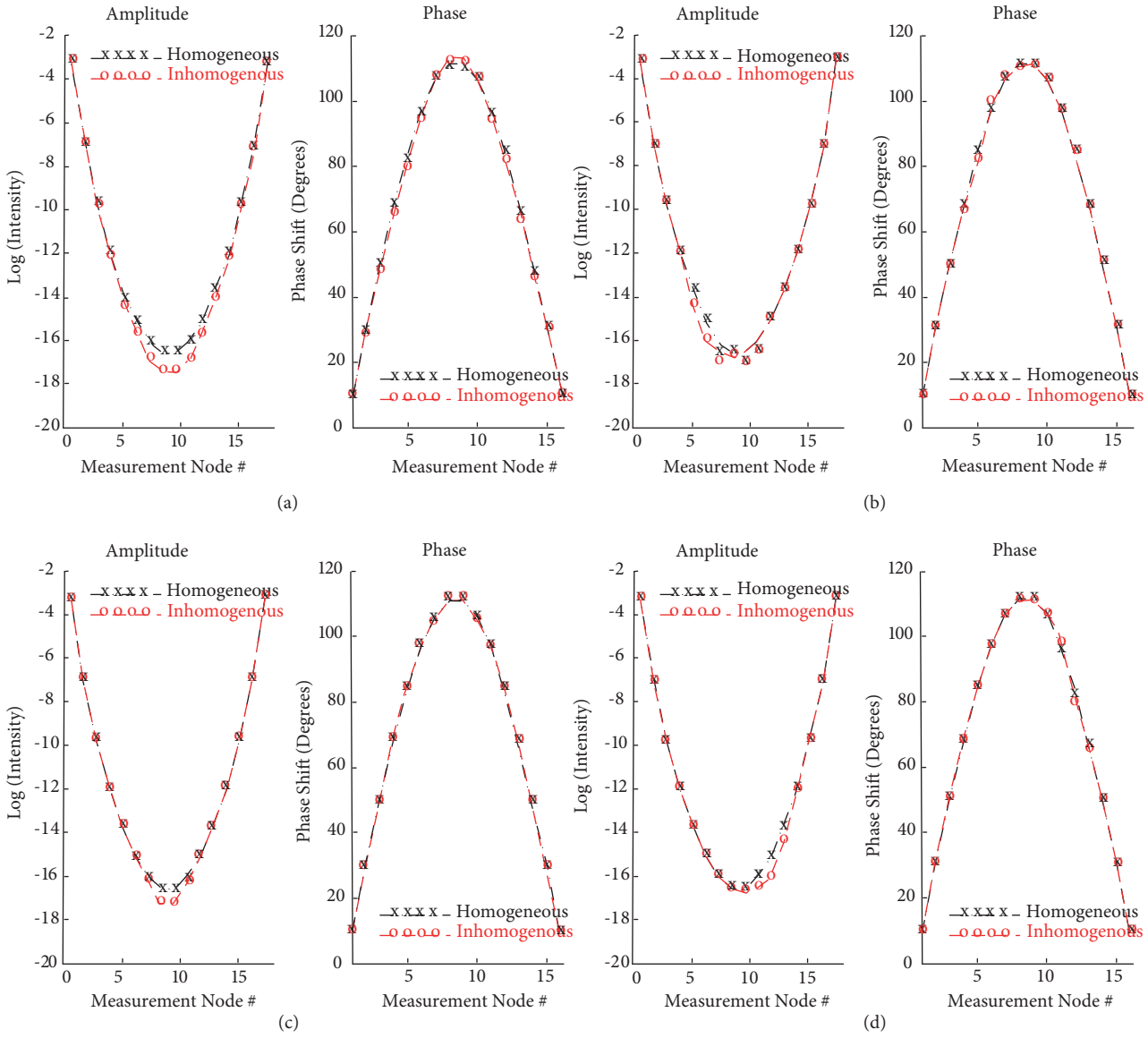

Figure 5. Same caption as Figure 4 but for $\mu_a = 0.02\,mm^{-1}$ and $\mu_s^{'} = 2\,mm^{-1}$ of inclusion.

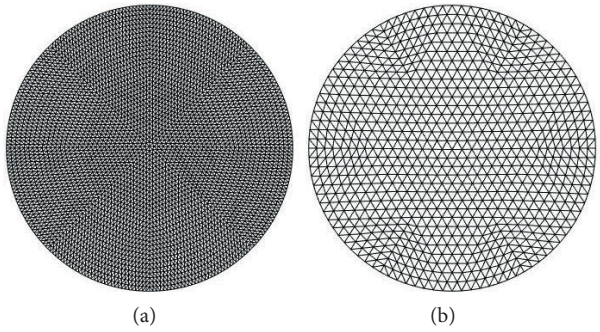

Figure 6. Finite element meshes of (a) the forward model and (b) the inverse model.

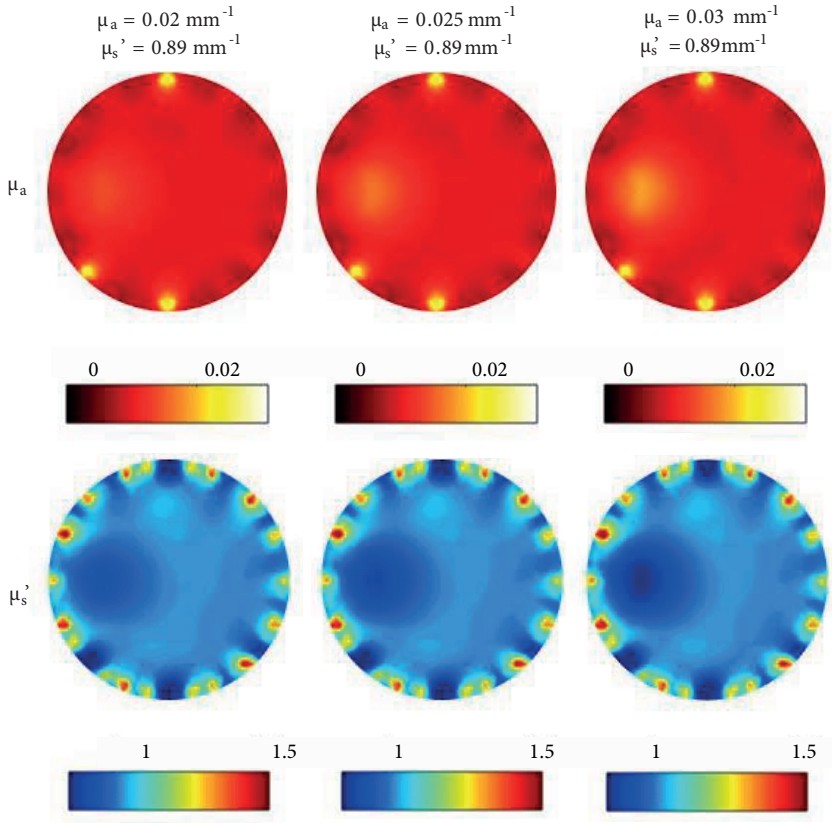

Figure 7. Simulated reconstructions of both the absorption and reduced scattering images for case A1.

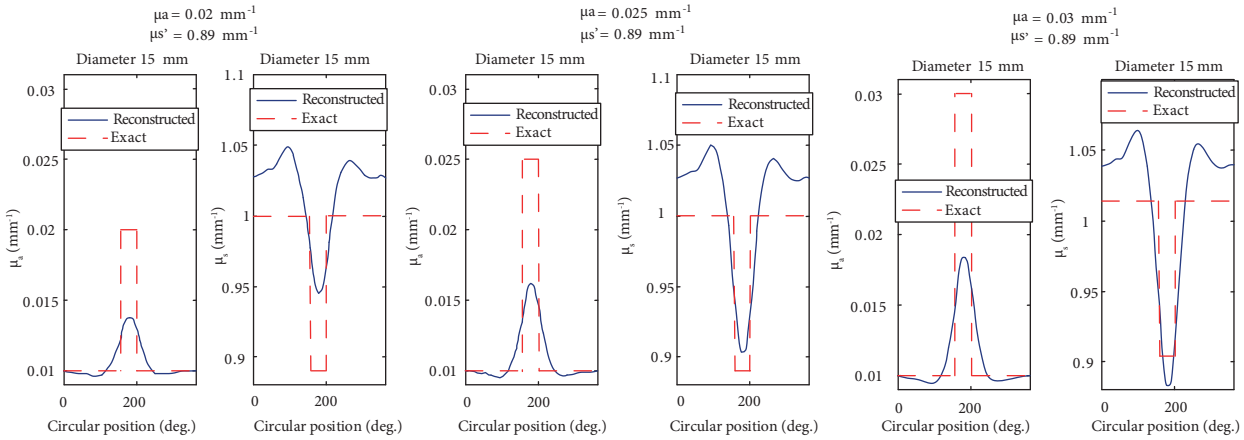

Figure 8. Comparison between exact (dotted line) and estimated (solid line) reconstruction line profiles with an inclusion radius of 15 mm for case A1.

We also provided a quantitative assessment for the reconstructed images between the FD proposed in this study and continuous wave (CW) [27] DOT using the structural similarity (SSIM) index [28]. The images in Figures 13 and 14 show the competitive performance of the CW algorithm for image reconstruction compared with the FD algorithm in Figures 7 and 9. Table 3 presents the evaluation results from calculating the SSIM

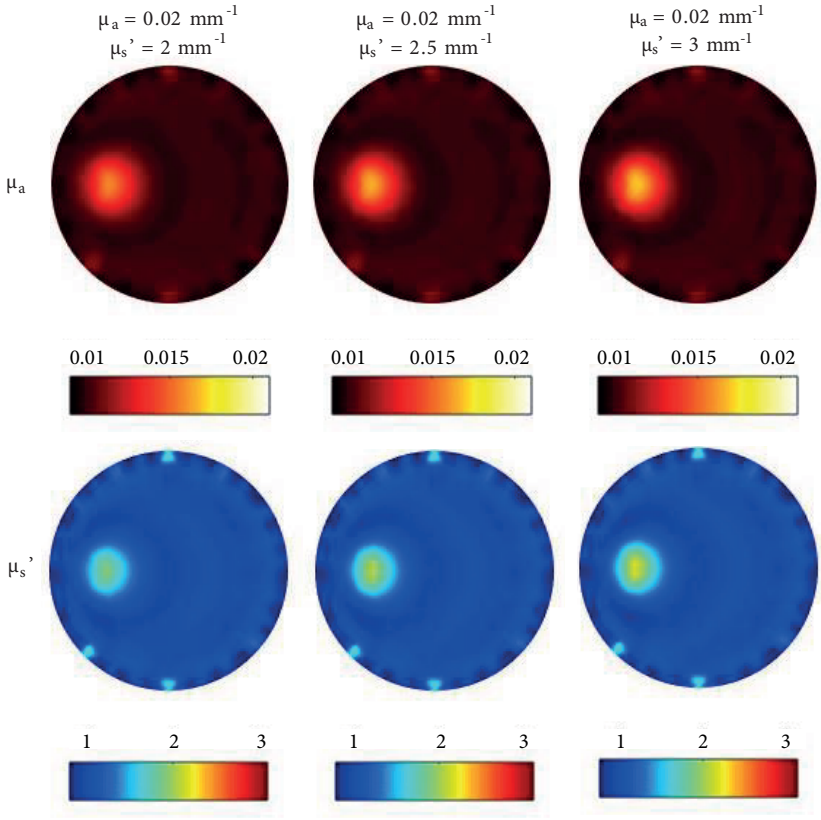

Figure 9. Same caption as Figure 7 but for case A2.

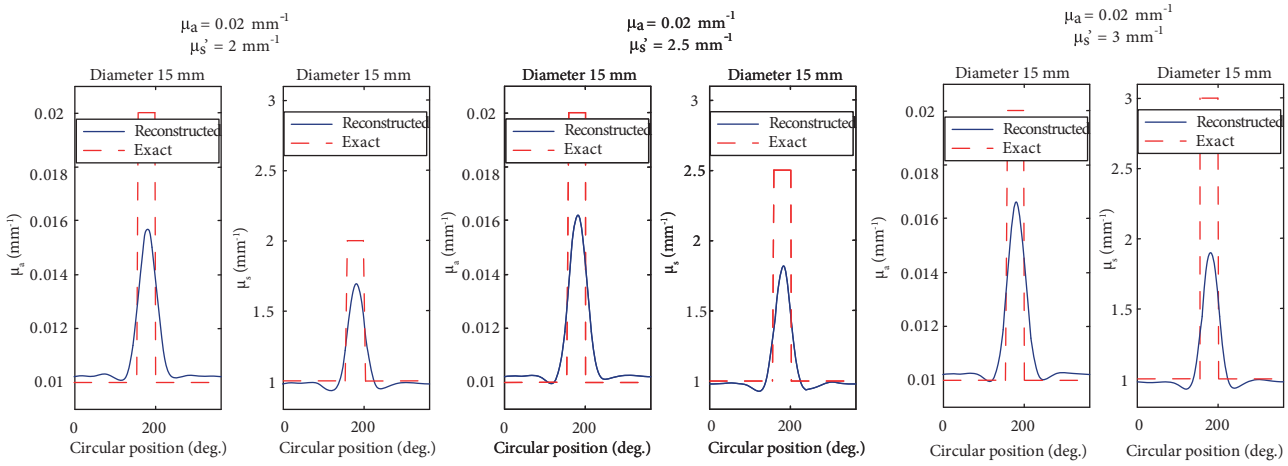

Figure 10. Same caption as Figure 8 but for case A2.

index for all images shown in Figures 7, 9, 13, and 14, where a numerical approach is used for assessing the quality of the reconstructed image when compared with the actual image of DOT through the whole parts. The image quality assessment in Table 3 verifies that the reconstructed optical property images using FD enhance the recovery of inclusion through considerable improvement in the inclusion contrast.

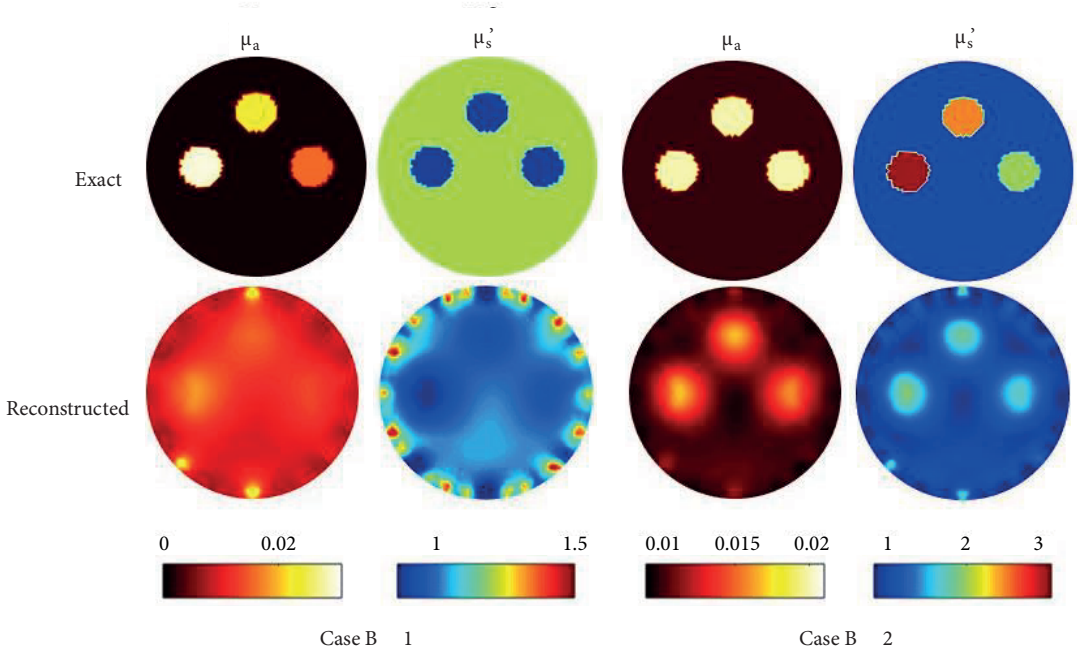

Figure 11. Same caption as Figure 7 but for three different inclusion locations and contrasts.

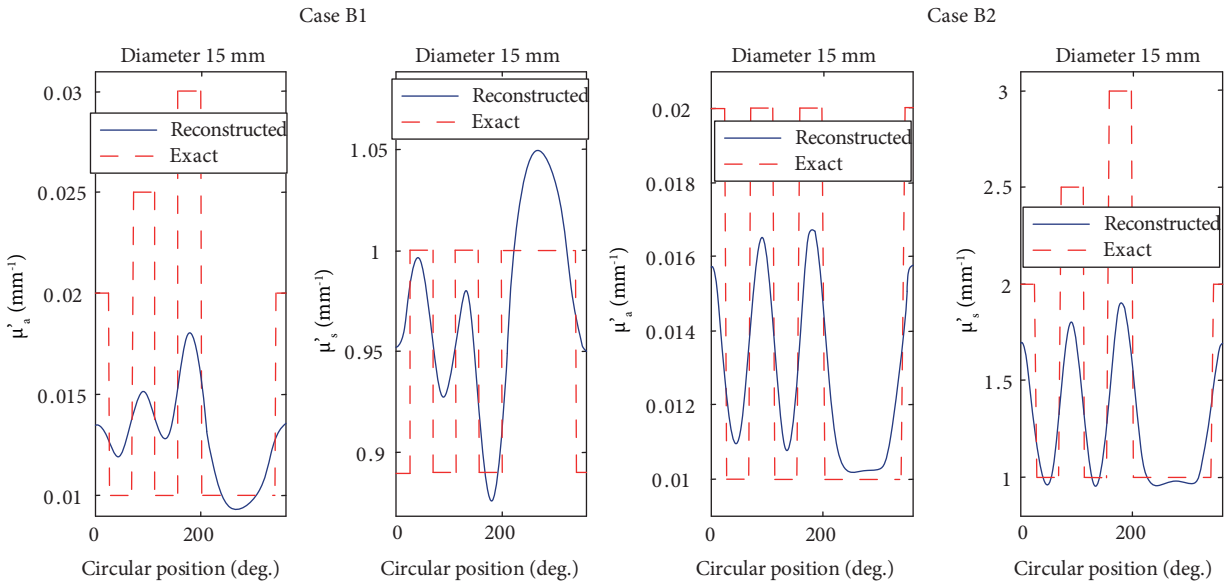

Figure 12. Same caption as Figure 8 but with three different inclusion locations.

4. Conclusions

In this study, a FEM-based image reconstruction algorithm of a DOT system has been proposed in the FD. Furthermore, Newton's method and TR are employed in the image reconstruction to improve the reconstructed images. For verifying the developed reconstruction algorithm, different designated simulation cases with different contrast ratios were used. According to image reconstruction results, they indicate that the reconstruction algorithm is feasible for breast examination for revealing the embedded tumor, where a tumor of 15 mm in

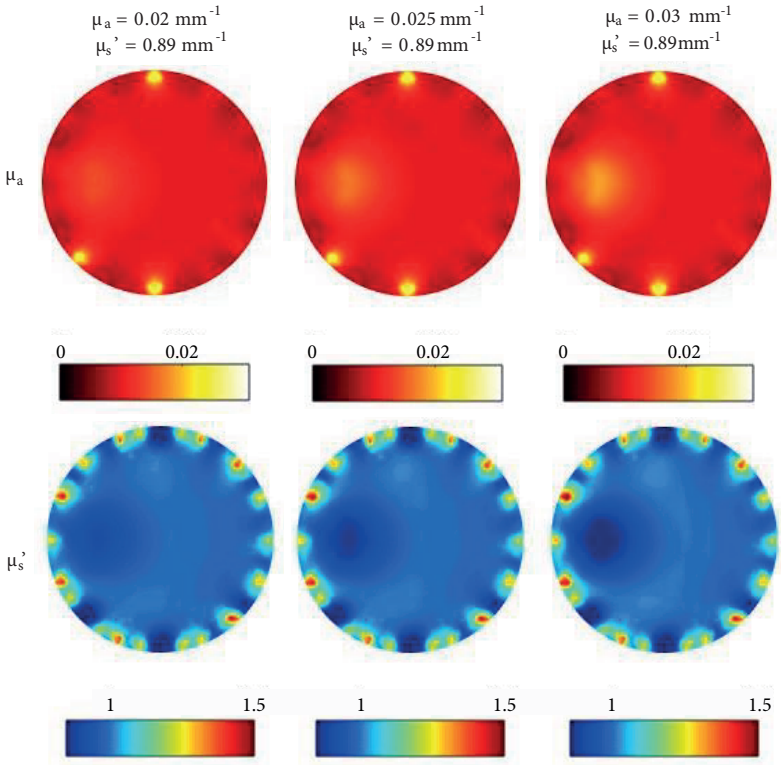

Figure 13. Same caption as Figure 7 using CW.

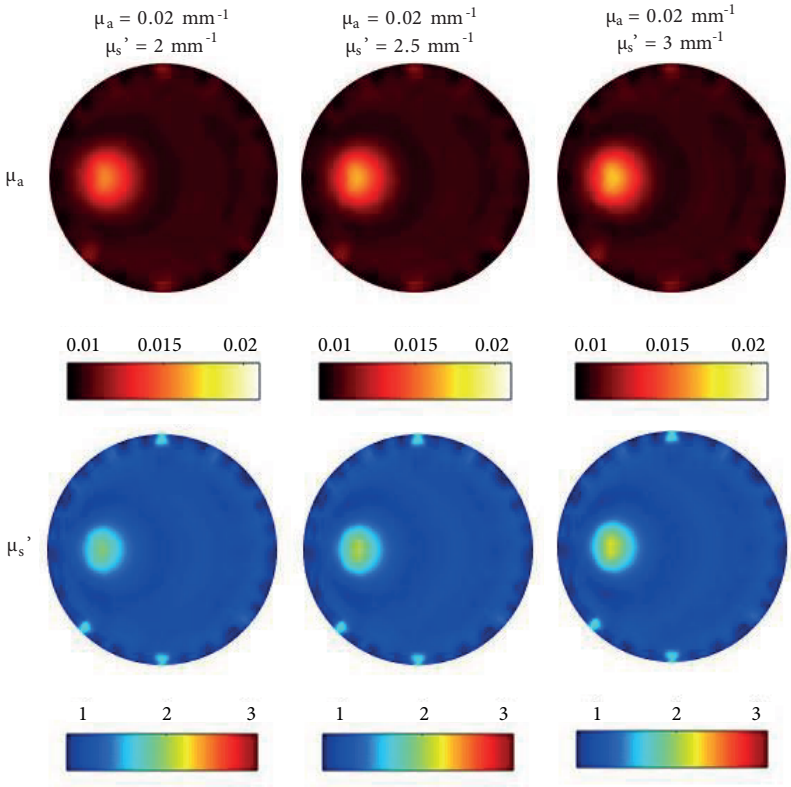

Figure 14. Same caption as Figure 7 but for case A2 using CW.

Table 3. Image quality evaluation with SSIM index for FD and CW.

$\mu_s^{'} = 0.89\,mm^{-1}$			$\mu_a = 0.02\,mm^{-1}$		
μ_a	SSIM		$\mu_s^{'}$	SSIM	
	FD	CW		FD	CW
$0.02\,mm^{-1}$	0.485	0.472	$2\,mm^{-1}$	0.712	0.700
$0.025\,mm^{-1}$	0.483	0.472	$2.5\,mm^{-1}$	0.689	0.671
$0.03\,mm^{-1}$	0.479	0.468	$3\,mm^{-1}$	0.634	0.613

diameter embedded in the model can be distinguished from the background. Overestimation or underestimation of optical properties' contrast occurred and could not be accurately determined; however, it remains effective for breast screening. Additionally, the SSIM index allows the image quality assessment for FD in this study and CW. The computational times of both methods for each iteration were similar, approximately 7–8 s, due to equal Jacobian matrix dimensions. Furthermore, it is expected that the image reconstruction algorithm here can be applied for experimental data, although the results displayed in this study have concentrated on the reconstructed images from simulated data.

References

[1] Bhowmik T, Liu H, Ye Z, Oraintara S. Dimensionality reduction based optimization algorithm for sparse 3-D image reconstruction in diffuse optical tomography. Sci Rep-Uk 2016; 6: 22242.

[2] Wang B, Wan W, Wang Y, Ma W, Zhang L, Li J, Zhou Z, Zhao H, Gao F. An L_p ($0 \leq p \leq 1$)-norm regularized image reconstruction scheme for breast DOT with non-negative-constraint. Biomed Eng Online 2017; 16: 32.

[3] Gibson A, Dehghani H. Diffuse optical imaging. Philos T R Soc A 2009; 367: 3055-3072.

[4] Leff DR, Warren OJ, Enfield LC, Gibson A, Athanasiou T, Patten DK, Hebden J, Yang GZ, Darzi A. Diffuse optical imaging of the healthy and diseased breast: a systematic review. Breast Cancer Res Tr 2008; 108: 9-22.

[5] Hebden JC, Arridge SR, Delpy DT. Optical imaging in medicine: I. Experimental techniques. Phys Med Biol 1997; 42: 825-840.

[6] Dehghani H, Srinivasan S, Pogue BW, Gibson A. Numerical modelling and image reconstruction in diffuse optical tomography. Philos T R Soc A 2009; 367: 3073-3093.

[7] Arridge SR, Schotland JC. Optical tomography: forward and inverse problems. Inverse Probl 2009; 25: 123010.

[8] Chen LY, Pan MC, Pan MC. Implementation of edge-preserving regularization for frequency-domain diffuse optical tomography. Appl Optics 2012; 51: 43-54.

[9] Bi B, Han B, Han W, Tang J, Li L. Image reconstruction for diffuse optical tomography based on radiative transfer equation. Comput Math Method M 2015; 2015: 286161.

[10] Chen LY, Pan MC, Pan MC. Flexible near-infrared diffuse optical tomography with varied weighting functions of edge-preserving regularization. Appl Optics 2013; 52: 1173-1182.

[11] Uludag K, Steinbrink J, Villringer A, Obrig H. Separability and cross talk: optimizing dual wavelength combinations for near-infrared spectroscopy of the adult head. Neuroimage 2004; 22: 583-589.

[12] Wu HY, Filer A, Styles I, Dehghani H. Development of a multi-wavelength diffuse optical tomography system for early diagnosis of rheumatoid arthritis: simulation, phantoms and healthy human studies. Biomed Opt Express 2016; 7: 4769-4786.

[13] Eames ME, Wang J, Pogue BW, Dehghani H. Wavelength band optimization in spectral near-infrared optical tomography improves accuracy while reducing data acquisition and computational burden. J Biomed Opt 2008; 13: 054037.

[14] Chen LY, Pan MCheng, Yan CC, Pan MChun. Wavelength band optimization in spectral near-infrared optical tomography improves accuracy while reducing data acquisition and computational burden. Appl Optics 2016; 55: 5729-5737.

[15] Zhang Q, Brukilacchio T, Li A, Stott J, Chaves T, Hillman E, Wu T, Chorlton M, Rafferty E, Moore R et al. Coregistered tomographic X-ray and optical breast imaging: initial results. J Biomed Opt 2005; 10: 024033.

[16] Yuan Z, Zhang Q, Sobel ES, Jiang H. Tomographic X-ray-guided three dimensional diffuse optical tomography of osteoarthritis in the finger joints. J Biomed Opt 2008; 13: 044006.

[17] Holboke M, Tromberg B, Li X, Shah N, Fishkin J, Kidney D, Butler J, Chance B, Yodh A. Three-dimensional diffuse optical mammography with ultrasound localization in a human subject. J Biomed Opt 2000; 5: 237-247.

[18] Zhu Q, Tannenbaum S, Hegde P, Kane M, Xu C, Kurtzman S. Noninvasive monitoring of breast cancer during neoadjuvant chemotherapy using optical tomography with ultrasound localization. Neoplasia 2008; 10: 1028-1040.

[19] Jiang Z, Piao D, Xu G, Ritchey JW, Holyoak GR, Bartels KE, Bunting CF, Slobodov G, Krasinki JS. Transrectal ultrasound-coupled near-infrared optical tomography of the prostate part ii: experimental demonstration. Opt Express 2008; 16: 17505-17520.

[20] Ntziachristos V, Yodh A, Schnall M, Chance B. MRI-guided diffuse optical spectroscopy of malignant and benign breast lesions. Neoplasia 2002; 4: 347-354.

[21] Dehghani H, Pogue B, Brooksby B, Srinivasan S, Paulsen K. In: 3rd IEEE International Symposium on Biomedical Imaging: Nano to Macro; 6–9 April 2006; Arlington, VA, USA. New York, NY, USA: IEEE. pp. 682-685.

[22] Vavadi H, Zhu Q. Automated data selection method to improve robustness of diffuse optical tomography for breast cancer imaging. Biomed Opt Express 2016; 7: 4007-4020.

[23] Guggenheim JA, Bargigia I, Farina A, Pifferi A, Dehghani H. Time resolved diffuse optical spectroscopy with geometrically accurate models for bulk parameter recovery. Biomed Opt Express 2016; 7: 3784-3794.

[24] Arridge SR, Schweiger M, Hiraoka M, Delpy DT. A finite element approach for modeling photon transport in tissue. Med Phys 1993; 20: 299-309.

[25] Pogue BW, Geimer S, McBride TO, Jiang S, Osterberg UL, Paulsen KD. Three-dimensional simulation of near-infrared diffusion in tissue: boundary condition and geometry analysis for finite-element image reconstruction. Appl Optics 2001; 40: 588-600.

[26] Jiang M, Zhou T, Cheng J, Cong W, Wang G. Image reconstruction for bioluminescence tomography from partial measurement. Opt Express 2007; 15: 11095-11116.

[27] Liu Y, Su J, Lin ZJ, Teng S, Rhoden A, Pantong N, Liu H. Reconstructions for continuous-wave diffuse optical tomography by a globally convergent method. J Appl Math Phys 2014; 2: 204-213.

[28] Wang Z, Bovik AC, Sheikh HR, Simoncelli EP. Image quality assessment: from error visibility to structural similarity. IEEE T Image Process 2004; 13: 600-612.